ADVANCED MATERIALS INTERFACES
www.advmatinterfaces.de

Passivation of Bi_2Te_3 Topological Insulator by Transferred CVD-Graphene: Toward Intermixing-Free Interfaces

Regina Galceran, Frédéric Bonell, Lorenzo Camosi, Guillaume Sauthier, Zewdu M. Gebeyehu, Maria José Esplandiu, Aloïs Arrighi, Iván Fernández Aguirre, Adriana I. Figueroa, Juan F. Sierra, and Sergio O. Valenzuela**

The investigation, and ultimate application, of topological insulators, typically involve exposure to ambient conditions or their integration with metals, which lead to surface oxidation or material intermixing. X-ray photoelectron spectroscopy (XPS) measurements that demonstrate passivated and intermixing-free interfaces in the topological insulator Bi_2Te_3 by means of dry-transferred CVD graphene are reported. After air exposure, no traces of Bi_2Te_3 oxidation are found. Furthermore, it is demonstrated that graphene acts as a very efficient metal and chalcogen diffusion barrier in Bi_2Te_3/graphene/permalloy (Py) heterostructures, which are relevant for spintronics. Such results are in stark contrast with the significant surface degradation observed in bare Bi_2Te_3 under ambient conditions and the deep Bi—Te bonding disruption that occurs in Bi_2Te_3/Py heterostructures. These findings provide a new approach to control and engineer topological insulator interfaces for spintronic applications and a new platform to investigate the combined use of graphene and topological insulator Dirac states.

1. Introduction

Device miniaturization and progress in nanotechnology have evidenced the crucial role of interfaces toward the performance of devices. Interface properties are relevant in all current spintronic technologies, as well as in many novel, potentially useful, spintronic phenomena and materials.[1–3] This is the case for topological insulators (TIs), which are characterized by insulating bulk and conductive topologically protected surface (or boundary) states (TSS). The TSS are of particular interest because of their spin-momentum locking, which constrains the electron spin orientation perpendicular to the electron momentum and represents an effective route for charge-to-spin interconversion (CSI). When a current is applied, the TSS generate a non-equilibrium spin density that can be used to manipulate the magnetization orientation of a ferromagnet (FM) by means of spin-orbit torques (SOTs), a key phenomenon for next-generation magnetic memory technologies.[2] Recent reports using TIs have demonstrated large SOT efficiencies.[4] However, to identify the microscopic mechanism of CSI and SOTs, as well as to maximize their efficiency, a deep understanding of the properties of the TI/FM interface is needed.[5–11]

Interface phenomena are complex, involving charge transfer, hybridization, intermixing, or alloying. More so when air-sensitive or reactive elements are involved, in which case, oxidation and intermixing are particularly relevant. Different strategies have been used to protect the surface of TIs from oxidation, from intercalation of Rb atoms[12] to Te capping (and latter decapping) for ex situ transfers of the TI.[13] In the case of TI/Py (Py = $Ni_{80}Fe_{20}$) heterostructures, an added challenge is the significant intermixing present: nickel was observed to diffuse into Bi_2Se_3, leading to phase separation,[7] and tellurium was found to diffuse out of Bi_2Te_3 deep into Py.[8] In these experiments, interface diffusion was reduced by intercalating thin nonmagnetic (metallic) spacers,[8] which were grown onto the TI before depositing the FM. However, it has been further established that interface modifications can alter the nature of the CSI mechanism, leading to large variations in the spin torque[8] and the CSI efficiency.[9,14,15]

R. Galceran, F. Bonell, L. Camosi, G. Sauthier, Z. M. Gebeyehu, M. J. Esplandiu, A. Arrighi, I. Fernández Aguirre, A. I. Figueroa, J. F. Sierra, S. O. Valenzuela
Catalan Institute of Nanoscience and Nanotechnology (ICN2)
CSIC and The Barcelona Institute of Science and Technology (BIST)
Campus UAB, Bellaterra, Barcelona 08193, Spain
E-mail: rgalceran@ub.edu; SOV@icrea.cat

F. Bonell
Univ. Grenoble Alpes, CNRS, CEA
Spintec, Grenoble 38000, France

Z. M. Gebeyehu, A. Arrighi, I. Fernández Aguirre
Universitat Autònoma de Barcelona
Bellaterra, Barcelona 08193, Spain

S. O. Valenzuela
Institució Catalana de Recerca i Estudis Avançats (ICREA)
Barcelona 08010, Spain

The ORCID identification number(s) for the author(s) of this article can be found under https://doi.org/10.1002/admi.202201997.

DOI: 10.1002/admi.202201997

Despite increasing efforts, and a variety of metal spacers investigated, interface control in TI/FM structures is still limited, while to our knowledge intermixing has never been completely suppressed. Because $(Bi,Sb)_2(Se,Te)_3$ family of TIs are van der Waals (vdW) materials, using another vdW material as a spacer represents an attractive alternative to the metals used so far. vdW materials are atomically smooth and, as part of a heterostructure, they tend to interact weakly, through vdW interaction, with minimal element intermixing. Among vdW materials, graphene is an excellent candidate as a diffusion barrier, given its closely packed hexagonal lattice, outstanding mechanical and thermal properties, and chemical stability. Graphene is known to be impermeable to standard gases, including helium,[16] and has been used to block the diffusion of metals, such as in Si/Cu,[17] Al/Si, and Au/Ni interfaces.[18] It has also been used to passivate Ni [19] and Cu and CuNi alloy,[20] although its effective long-term passivation of Cu is controverted.[21–25] Some studies report a lack of passivation or even increased oxidation,[22,23] possible explanations including the presence of defects in graphene [24,26] or reversible oxygen intercalation at the graphene-Cu interface.[21] Long-term passivation of FMs such as Ni and Co by direct chemical vapor deposition (CVD) of graphene has also been reported,[27] and used as electrodes in magnetic tunnel junctions.[28–30] In fact, the interaction between the graphene and the FM leads to hybridization (chemisorption or physisorption), both potentially useful for spintronic applications.[31] In addition, although TI/graphene/FM heterostructures have not been investigated experimentally, giant CSI and large SOTs have been predicted.[32]

In this work, we fabricated Bi_2Te_3/graphene and Bi_2Te_3/graphene/FM heterostructures in order to investigate the performance of graphene as both an oxidation and diffusion barrier. By means of X-ray photoelectron spectroscopy (XPS) we demonstrate that graphene prevents Bi_2Te_3 from oxidizing, even after exposure to ambient air and moisture. A Py film was then grown under ultra-high vacuum (UHV), forming a Bi_2Te_3/graphene/Py heterostructure. The chemical states of Te and Bi in the Bi_2Te_3 film were investigated by XPS and compared with results obtained with Bi_2Te_3/Py and Bi_2Te_3. Our systematic analysis found no trace of intermixing when graphene is intercalated, demonstrating its superior diffusion barrier performance for Ni and Te.

2. Results and Discussion

2.1. TI/Graphene Heterostructure

Figure 1 shows a schematic of the developed approach to fabricate TI/graphene heterostructures (see the Experimental Section for details on each step). The topological insulator, Bi_2Te_3, was grown by molecular beam epitaxy[33] (MBE) on a BaF_2(111) substrate and transferred, using a UHV suitcase, to a glovebox with inert Ar gas, where the O_2 and the H_2O concentrations were below 1 ppm. In order to achieve a large-area scalable process, graphene was grown by CVD on a Cu foil.[34] Dry graphene stamps were prepared using a bilayer of polypropylene carbonate (PPC) and polydimethylsiloxane (PDMS),

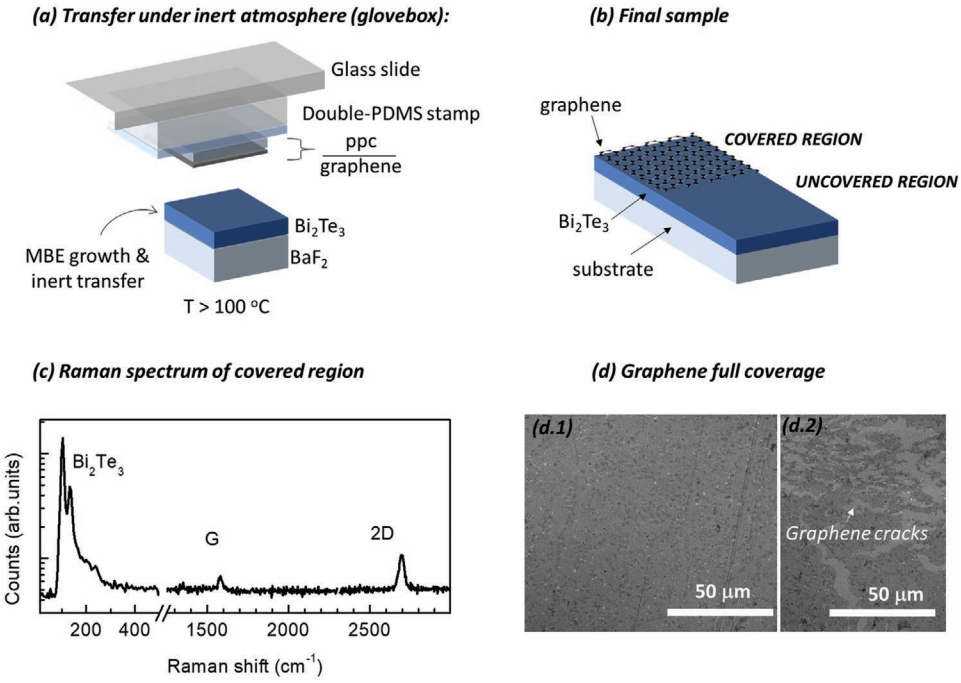

Figure 1. Sketch of the sample fabrication process and basic characterization. a) A dry stamp of PDMS/PPC/graphene was introduced into the glovebox and pressed onto the sample (graphene facing down) while the latter was heated to over 100 °C to melt the PPC; b) after cleaning the resist, the final sample allowed for comparison between regions with and without graphene coverage. c) Raman spectrum confirmed the presence of graphene on the covered region, using a laser wavelength of 488 nm. d) SEM images reveal graphene full coverage in the majority of the transferred area (as in 1d1) as opposed to visible graphene discontinuities (cracks) formed during non-optimized transfer (shown as reference in 1d2).

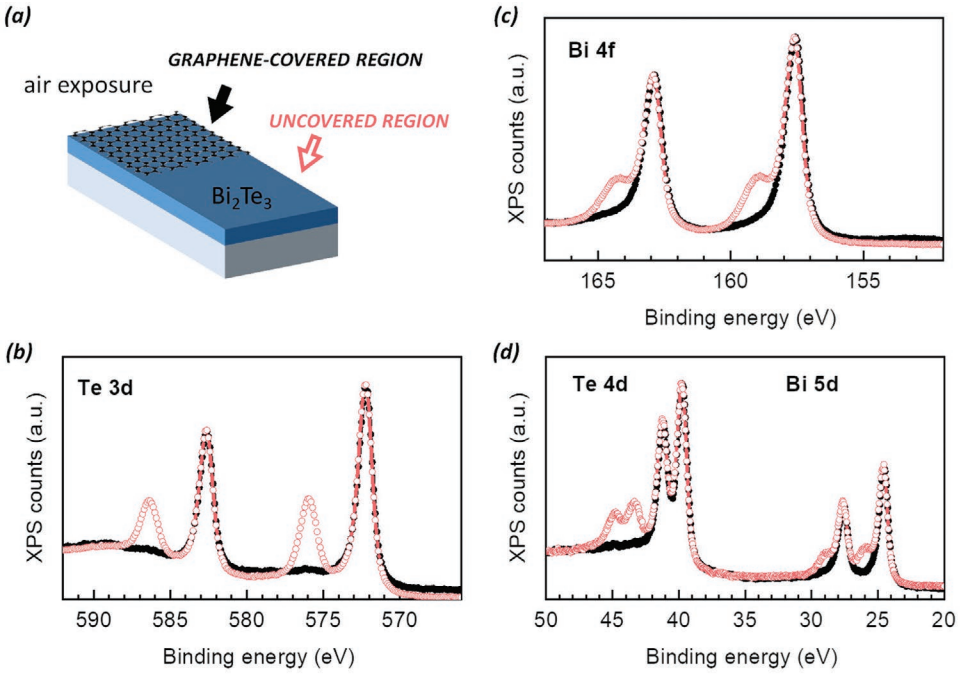

Figure 2. XPS measurements comparing the regions with and without graphene coverage (closed black and open red symbols, respectively). Te 3d, Bi 4f, Bi 5d, and Te 4d peaks are shown in the panels (b–d) as labeled. In all cases, large oxide peaks are present in the areas without graphene. Such peaks are absent for the graphene-capped area. Spectra intensities have been shifted and normalized to the value of the maximum of the largest peak.

followed by the removal of the Cu foil by means of wet etching. The graphene stamp and Bi_2Te_3 were put in contact using an optical microscope and micro-positioners (Figure 1a). The whole stack was then heated to over 100 °C to melt the PPC and transfer the graphene/PPC onto Bi_2Te_3. Up to this point, the process was carried out in the glovebox to avoid oxidation of the Bi_2Te_3 surface. Afterwards the sample was taken out of the glove box, the PPC was removed with acetone and isopropanol, and then the bilayer was exposed to air for over an hour. In the finished sample, graphene covered Bi_2Te_3 only partially to enable a direct comparison between regions with and without graphene coverage in the same Bi_2Te_3 film (Figure 1b).

Poor contrast using an optical microscope makes it difficult to distinguish the quality of the graphene, or even its presence, on the Bi_2Te_3. However, this can be readily achieved with Raman spectroscopy. The Raman spectrum presented in Figure 1c shows the two characteristic peaks for Bi_2Te_3 at low frequencies (Raman shift < 400 cm^{-1}), while the presence of graphene is confirmed by means of the G and 2D peaks, visible at larger frequencies (≈1600 cm^{-1} and ≈2700 cm^{-1}). The faint D peak at ≈1350 cm^{-1} demonstrates the successful transfer of good-quality graphene with a relatively low density of defects. Scanning electron microscope (SEM) images also confirm full continuous graphene coverage over the majority of the transferred area when using an optimized transfer process (Figure 1d.1). This contrasts with the visible graphene cracks present in regions of samples for which the transfer process was not optimal (Figure 1d.2).

2.2. Graphene as Oxidation, Passivation Barrier

Figure 2 compares XPS measurements for Bi_2Te_3 over regions with and without graphene coverage (black-solid and red-open symbols, respectively). The direct comparison of the two regions (represented in Figure 2a) allows us to eliminate any characterization artifacts associated with air-exposure time and ambient conditions, as well as any possible variation in the morphology of the grown Bi_2Te_3 films.

The XPS spectra reveal peaks at the Te 3d (Figure 2b), Bi 4f (Figure 2c), and Te 4d and Bi 5d (Figure 2d) edges. Several peaks in Figure 2b,c are directly associated to Bi_2Te_3, located at 572.2 eV (Te $3d^{5/2}$), 582.6 eV (Te $3d^{3/2}$), 157.6 eV (Bi $4f^{7/2}$) and 162.9 eV (Bi $4f^{5/2}$). Additional peaks are observed only in bare Bi_2Te_3 at larger binding energies (575.9 and 586.4 eV for Te and 158.8 and 164.1 eV for Bi) and are indicative of substantial oxidation. By fitting the areas of the Bi, Te and their corresponding oxides, and considering electron escape depths of λ_{Bi} = 2.3 nm[35] and λ_{Te} = 2.1 nm,[36] we estimate the oxide thickness to be ≈1.3 nm and 0.7 nm for Bi and Te, respectively (see Experimental Section for more details). This is in stark contrast with the Bi_2Te_3/graphene region, in which no oxidation is discernable. An equivalent analysis, yielding the same conclusion, can be carried out in the Te 3d and Bi 5d edges (Figure 2d). Note that the spot size of the XPS is in the few mm range, confirming that the graphene transfer has been successful and that the TI passivation is effective over a large area.

Additional angle-resolved photoemission spectroscopy measurements (see Supplementary Information) on the

Bi_2Te_3/graphene heterostructure show visible TSS of the TI and slight electron doping. However, n-doping cannot be unambiguously attributed to the presence of the graphene capping layer. Such doping has been reported to increase over time in in situ cleaved TIs, even while maintaining the sample inside UHV conditions.[37]

The successful fabrication of TI/graphene heterostructures by dry transferring CVD graphene, while preventing oxidation, is an important milestone. Such heterostructures have attracted significant attention as an electronic platform to combine low-energy Dirac states with very distinct properties and due to the potential to enhance the spin-orbit coupling of graphene by proximity phenomena with the TI.[38–44] Because exposure to ambient conditions causes surface oxidation in the $(Bi,Sb)_2(Te,Se)_3$ TIs,[45–48] many experimental studies using these materials aimed at minimizing the time of exposure to air[41,43] or to water-based solutions during graphene transfer.[49] However, despite these efforts, some degree of surface modification or oxidation is unavoidable.[45–48] Alternative strategies, such as the deposition of the TI on graphene (either epitaxially grown[50] or exfoliated[51,52]), have also been adopted. However, the characterization of these heterostructures must be carried out through transport experiments, as access to the buried interface is not possible, unless the substrate is removed.[40]

2.3. TI/Graphene/FM Heterostructure: Graphene as Intermixing/Diffusion Barrier

After confirming the lack of oxidation of Bi_2Te_3 with a graphene barrier, a bilayer of Py(2 nm)/Al(2 nm) was grown on top of Bi_2Te_3/graphene in UHV (see Experimental Section for details). The Py and Al layers were made thin enough to be able to probe the composition and chemical state of the buried TI. XPS is a surface-sensitive technique; the escape depth of the photoelectrons in most metals is ≈2–5 nm and thus, the XPS signal would be strongly suppressed for larger thicknesses.

Figure 3 shows XPS spectra around the binding energies of the $Bi4f^{7/2}$ and $Te3d^{5/2}$ edges. The results for Bi_2Te_3/graphene/Py are plotted with blue symbols (top trace) while those for Bi_2Te_3/Py are plotted with green symbols (middle trace). Additional measurements for pure Bi and Te (black) and for Bi_2Te_3 (red) and Bi_2Te_3/graphene (orange) are shown as references. The emission lines for bare Bi_2Te_3 at 572.2 eV ($Bi4f^{7/2}$) and 157.6 eV ($Te3d^{5/2}$) are indicated with red solid vertical lines; those for pure Bi and Te at 156.9 eV and at 573.0 eV, respectively, are indicated with black dotted vertical lines. The observed energy shift of 0.7-0.8 eV in Bi_2Te_3, which is opposite for $Bi4f^{7/2}$ and $Te3d^{5/2}$ in relation to the pure elements, is due to the charge transfer occurring in the Bi-Te covalent bonds within the TI.

The emission lines in Bi_2Te_3/Py are very different from those in Bi_2Te_3, having instead the same binding energies that characterize pure Bi and Te. As previously reported,[8] this is the result of a strong modification of the chemical Bi-Te bonding in Bi_2Te_3 upon deposition of Py. Angular XPS measurements have shown that Te diffuses out of Bi_2Te_3 leaving a Bi-rich interface.[8] In stark contrast, both Bi_2Te_3/graphene and Bi_2Te_3/graphene/Py maintain the exact peak positions of Bi_2Te_3, demonstrating that all detected Bi and Te remain in Bi_2Te_3 and no broken Bi-Te bonds are present. This is a notable result given the large affinity of Py for Te.[8] Suppression of the intermixing has been achieved by intercalating aluminum, silver, and Te between Bi_2Te_3 and Py. However, the observed suppression with these materials is only partial, even with several nanometers of Te, as concluded from the coexistence of the bare Bi_2Te_3 and pure Bi and Te emission lines in those heterostructures.[8] The complete suppression of intermixing in Bi_2Te_3/graphene/Py, as demonstrated in Figure 3 and observed here for the first time, therefore represents a remarkable improvement with respect to metallic interlayers.

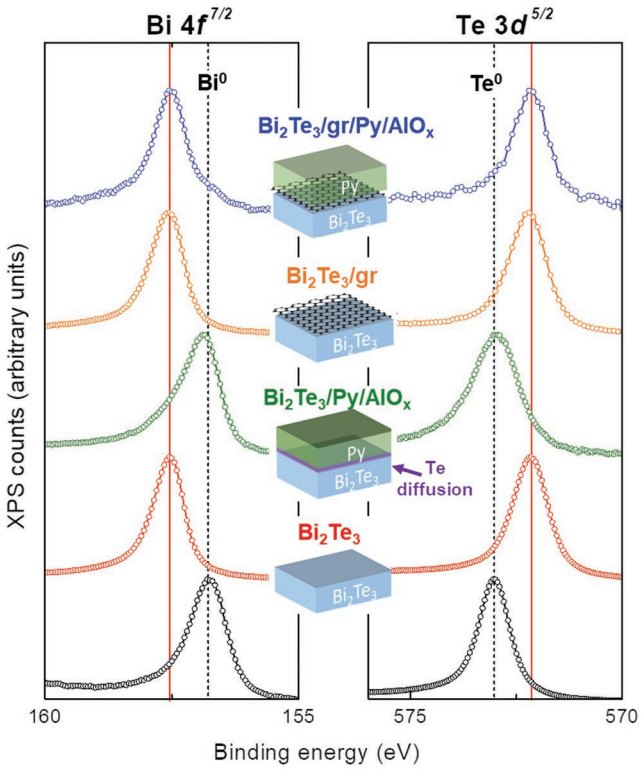

Figure 3. X-ray photoemission spectroscopy at the Bi $4f^{7/2}$ and Te $3d^{5/2}$ peaks for different stacks with and without graphene interlayer. From bottom to top: pure Bi^0 and Te^0 (black symbols), Bi_2Te_3 (red symbols), in situ grown Bi_2Te_3/Py/AlO_x (green symbols), Bi_2Te_3/graphene (orange symbols) and Bi_2Te_3/graphene/Py/AlO_x (blue symbols). The peak positions for pure Bi^0 and Te^0 (dotted black line), as well as those corresponding to Bi_2Te_3 (solid red line), are indicated as references. Data from samples not containing graphene was taken from reference [8].

3. Conclusion

We have prepared Bi_2Te_3/graphene heterostructures by dry transferring CVD-grown graphene onto MBE-grown Bi_2Te under an inert atmosphere. We have shown that the graphene layer effectively passivates the Bi_2Te_3 surface, even after exposure to ambient conditions, as the XPS spectra show no traces of surface oxidation.

In addition to surface passivation, graphene acts as a very efficient metal and chalcogen diffusion barrier in relevant Bi_2Te_3/graphene/Py heterostructures. By means of XPS

measurements, we show that the chemical bonding of the Bi_2Te_3 remains intact after depositing Py on top of graphene. This result contrasts with the deep Bi—Te bonding disruption observed in Bi_2Te_3/Py heterostructures, or even when selected metallic interlayers are inserted between Bi_2Te_3 and Py.

Our heterostructure fabrication method does not require substrate-dependent growth optimization and allows for large-scale samples. Even though the passivation of the surface and intermixing-free interfaces are demonstrated for Bi_2Te_3, we expect similar results for the whole family of $(Bi,Sb)_2(Se,Te)_3$ TI materials. Considering the increasing interest in quantum transport in TIs and graphene, in proximity effects, and in spintronic applications relying on TI/FM interfaces, our results offer important prospects for fundamental progress and for future spintronics. Regarding spintronics, future work should focus on the properties of the ferromagnet, which is grown on the TI/graphene bilayer, and, for example, the efficiency of the spin-orbit torques in the finished heterostructure.

4. Experimental Section

TI Film Growth: Bi_2Te_3 films with a thickness of ten quintuple layers (10 nm) were grown by co-evaporation of Bi and Te in an MBE chamber with a base pressure of 2×10^{-10} mbar. The growth rate was ≈0.25 nm min^{-1}. The fluxes were previously measured with a quartz crystal microbalance. The substrates used, BaF_2 (111) purchased at PIKEM, were previously outgassed in UHV at 800 °C for 1 h (in the same chamber) and the growth was done at 380 °C and monitored by in situ reflection high energy electron diffraction. Films were transferred, using a vacuum suitcase (≈10^{-8} mbar), to a glovebox under Ar atmosphere, where the O_2 and the H_2O concentrations were below 1 ppm. There, graphene was transferred on top, as described in the main text. The sample temperature given here was the temperature measured with a thermocouple located between the heater and the sample holder, leading to an overestimation of the real temperature, which correspond to ≈575 °C for the degassing and 260 °C for the growth.

Graphene Growth and Stamp Preparation: Graphene was grown on a 25 µm thick Cu foil (99.8% or 99.999% Alfa Aesar) by CVD using a Lindberg/Blue tube furnace. The copper foil was first cleaned in acetone and isopropanol and then electropolished in an electrochemical cell by applying 3 V for 90 s and using the copper foil as anode. The electrolyte solution was a mixture of 150 mL of water, 75 mL of phosphoric acid, 75 mL of ethanol, 15 mL of isopropanol, and 1.5 g of urea.[53] After that, the polished Cu foil was annealed in Ar (450 sccm) and H_2 (50 sccm) for 45 min under low pressure (base pressure of 20 mbar). Graphene was then grown using a CH_4 flow of 30 sccm at 1000 °C for 10 min and keeping the same flow conditions for H_2 and Ar as in the annealing step. These growth conditions produce a full multidomain graphene monolayer and also occasionally small domains of bilayer graphene at the center of the individual graphene domains.[54] For graphene transfer process, four layers of polypropylene carbonate (PPC) (at a concentration of 0.1 gr mL^{-1}) were spin-coated on top of the graphene and heated to 80 °C during 1 min after each layer. Finally, a thicker polydimethylsiloxane (PDMS) film was attached to the surface of the PPC, to later provide support with the handling of the stamp. Cu was wet-etched with diluted ammonium persulfate (0.25 M) and rinsed with water as was standard procedure[55]. The PDMS stamp with graphene was left to dry overnight and entered into the glovebox.

Py/Al deposition: After the characterization of the Bi_2Te_3/graphene surface, the sample was reintroduced in the MBE chamber. The sample was outgassed at 280 °C for 1 h in UHV and cooled down to liquid nitrogen temperature for the evaporation of Py (2 nm) and Al (2 nm) with effusion cells at growth rates of ≈0.24 and 0.15 nm min^{-1}, respectively. The thickness was monitored with a calibrated quartz crystal microbalance. After growth, the sample was taken out to air for the oxidation of the Al into AlO_x.

Raman measurements: Raman spectra were taken using a Witec Alpha300 R confocal Raman spectrometer and the 488 nm laser line, using a power of 0.8 mW. The spectra were measured with 100× magnification. The grating used for probing the graphene peaks was 600 lines mm^{-1}, while a grating of 1800 lines mm^{-1} was used for higher resolution to investigate the spectra for Bi_2Te_3.

XPS measurements: After exposure to air, samples were introduced into a UHV chamber (10^{-10} mbar), and XPS was carried out using a SPECS PHOIBOS hemispherical analyzer with a monochromatized X-ray source (al K_α line of 1486.6 eV, 300 W). Calibration was done using the C 1s peak as reference. For the measurement of the non-oxidized Bi_2Te_3 surface, the film was grown in the MBE and capped by a Te layer (15 nm) deposited in situ below 100 °C. Inside the XPS chamber, the Te capping layer was desorbed by heating the sample up to 190 °C for 10 min. For the sample with and without graphene coverage (Bi_2Te_3/graphene), no previous annealing was done prior to the XPS measurements. No change was observed in the XPS peak positions after annealing at 300 °C for 30 min, just an increase in their intensity. To estimate the oxide thickness, it was noted that Bi_2Te_3 was much thicker than the electron escape depth. This led to $\frac{I_{ox}}{I_{non-ox}} \approx 1 - \exp\left(-\frac{t_{ox}}{\lambda}\right)$, where I_{ox} and I_{non-ox} are the peak areas corresponding to the oxidized and non-oxidized elements (Te or Bi), respectively. As stated in the main text, $\lambda = 2.3$ nm (2.1 nm) was taken at the Bi 4f (Te 3d) energy.[35] The analysis performed separately at the Bi 4f and Te 3d lines yielded oxide thicknesses of 1.3 nm and 0.7 nm for Bi and Te, respectively.

Supporting Information

Supporting Information is available from the Wiley Online Library or from the author.

Acknowledgements

The authors acknowledge the support of the Spanish Research Agency (AEI), Ministry of Science and Innovation (MCIN) under contract no. PID2019-111773RB-I00/AEI/10.13039/501100011033, PGC2018-095032-B-100, and SEV-2017-0706 Severo Ochoa, and by PCI2021-122035-2A funded by MICIN and by the European Union Next Generation EU/PRTR, and of the European Union's Horizon 2020 under grant agreement 881603 (Graphene Flagship). R.G. acknowledges funding from the European Union's Horizon 2020 research and innovation program under the Marie Sklodowska-Curie grant agreement No 840588 (GRISOTO) and I.F.A from a fellowship from la Caixa Foundation (ID 100010434) with code LCF/BQ/DI18/11660030 and of H2020 Marie Skłodowska-Curie grant agreement No. 713673. J.F.S acknowledges support from MINECO under contract RYC2019-028368-I/AEI/10.13039/50110001103.

Conflict of Interest

The authors declare no conflict of interest.

Data Availability Statement

The data that support the findings of this study are available from the corresponding author upon reasonable request.

Keywords

Bi_2Te_3, graphene–topological insulator interface, intermixing, passivation, XPS

Received: September 8, 2022
Revised: October 30, 2022
Published online: December 6, 2022

[1] I. Žutić, J. Fabian, S. das Sarma, *Rev. Mod. Phys.* **2004**, *76*, 446.
[2] B. Dieny, I. L. Prejbeanu, K. Garello, P. Gambardella, P. Freitas, R. Lehndorff, W. Raberg, U. Ebels, S. O. Demokritov, J. Akerman, A. Deac, P. Pirro, C. Adelmann, A. Anane, A. v. Chumak, A. Hirohata, S. Mangin, S. O. Valenzuela, M. C. Onbaşlı, M. d'Aquino, G. Prenat, G. Finocchio, L. Lopez-Diaz, R. Chantrell, O. Chubykalo-Fesenko, P. Bortolotti, *Nat. Electron.* **2020**, *3*, 446.
[3] J. F. Sierra, J. Fabian, R. K. Kawakami, S. Roche, S. O. Valenzuela, *Nat. Nanotechnol.* **2021**, *16*, 856.
[4] C.-F. Pai, *Nat. Mater.* **2018**, *17*, 755.
[5] V. P. Amin, P. M. Haney, M. D. Stiles, *J Appl Phys* **2020**, *128*, 151101.
[6] R. Galceran, B. Tian, J. Li, F. Bonell, M. Jamet, C. Vergnaud, A. Marty, J. H. García, J. F. Sierra, M. v. Costache, S. Roche, S. O. Valenzuela, A. Manchon, X. Zhang, U. Schwingenschlögl, *APL Mater.* **2021**, *9*, 100901.
[7] S.-J. Chang, P.-Y. Chuang, C.-W. Chong, Y.-J. Chen, J.-C. A. Huang, P.-W. Chen, Y.-C. Tseng, *RSC Adv.* **2018**, *8*, 7785.
[8] F. Bonell, M. Goto, G. Sauthier, J. F. Sierra, A. I. Figueroa, M. V. Costache, S. Miwa, Y. Suzuki, S. O. Valenzuela, *Nano Lett.* **2020**, *20*, 5893.
[9] E. Longo, L. Locatelli, M. Belli, M. Alia, A. Kumar, M. Longo, M. Fanciulli, R. Mantovan, *Adv. Mater. Interfaces* **2021**, *8*, 2101244.
[10] E. Rongione, S. Fragkos, L. Baringthon, J. Hawecker, E. Xenogiannopoulou, P. Tsipas, C. Song, M. Mičica, J. Mangeney, J. Tignon, T. Boulier, N. Reyren, R. Lebrun, J. M. George, P. le Fèvre, S. Dhillon, A. Dimoulas, H. Jaffrès, *Adv. Opt. Mater.* **2022**, *10*, 2102061.
[11] E. Longo, M. Belli, M. Alia, M. Rimoldi, R. Cecchini, M. Longo, C. Wiemer, L. Locatelli, P. Tsipas, A. Dimoulas, G. Gubbiotti, M. Fanciulli, R. Mantovan, *Adv. Funct. Mater.* **2022**, *32*, 2109361.
[12] M. Bianchi, R. C. Hatch, Z. Li, P. Hofmann, F. Song, J. Mi, B. B. Iversen, Z. M. Abd El-Fattah, P. Löptien, L. Zhou, A. A. Khajetoorians, J. Wiebe, R. Wiesendanger, J. W. Wells, *ACS Nano* **2012**, *6*, 7009.
[13] G. Kremer, K. Zhu, T. Pierron, V. Fournee, J. Ledieu, S. Andrieu, B. Kierren, L. Moreau, D. Malterre, K. He, Q. K. Xue, Y. Fagot-Revurat, Y. Lu, *J Phys D Appl Phys* **2019**, *52*, 494002.
[14] R. Sun, S. Yang, X. Yang, E. Vetter, D. Sun, N. Li, L. Su, Y. Li, Y. Li, Z.-Z. Gong, Z.-K. Xie, K.-Y. Hou, Q. Gul, W. He, X.-Q. Zhang, Z.-H. Cheng, *Nano Lett.* **2019**, *19*, 31.
[15] H. He, L. Tai, D. Wu, H. Wu, A. Razavi, K. Wong, Y. Liu, K. L. Wang, *APL Mater.* **2021**, *9*, 071104.
[16] J. S. Bunch, S. S. Verbridge, J. S. Alden, A. M. van der Zande, J. M. Parpia, H. G. Craighead, P. L. McEuen, *Nano Lett.* **2008**, *8*, 2458.
[17] J. Hong, S. Lee, S. Lee, H. Han, C. Mahata, H. W. Yeon, B. Koo, S. il Kim, T. Nam, K. Byun, B. W. Min, Y. W. Kim, H. Kim, Y. C. Joo, T. Lee, *Nanoscale* **2014**, *6*, 7503.
[18] H.-Y. Kim, C. Lee, J. Kim, F. Ren, S. J. Pearton, *J. Vac. Sci. Technol., B* **2012**, *30*, 030602.
[19] Y. S. Dedkov, M. Fonin, C. Laubschat, *Appl. Phys. Lett.* **2008**, *92*, 052506.
[20] S. Chen, L. Brown, M. Levendorf, W. Cai, S. Y. Ju, J. Edgeworth, X. Li, C. W. Magnuson, A. Velamakanni, R. D. Piner, J. Kang, J. Park, R. S. Ruoff, *ACS Nano* **2011**, *5*, 1321.
[21] P. R. Kidambi, B. C. Bayer, R. Blume, Z. J. Wang, C. Baehtz, R. S. Weatherup, M. G. Willinger, R. Schloegl, S. Hofmann, *Nano Lett.* **2013**, *13*, 4769.
[22] M. Schriver, W. Regan, W. J. Gannett, A. M. Zaniewski, M. F. Crommie, A. Zettl, *ACS Nano* **2013**, *7*, 5763.
[23] F. Zhou, Z. Li, G. J. Shenoy, L. Li, H. Liu, *ACS Nano* **2013**, *7*, 6939.
[24] D. Prasai, J. C. Tuberquia, R. R. Harl, G. K. Jennings, K. I. Bolotin, *ACS Nano* **2012**, *6*, 1102.
[25] C. G. Kang, S. K. Lim, S. Lee, S. K. Lee, C. Cho, Y. G. Lee, H. J. Hwang, Y. Kim, H. J. Choi, S. H. Choe, M. H. Ham, B. H. Lee, *Nanotechnology* **2013**, *24*, 115707.
[26] Y. P. Hsieh, M. Hofmann, K. W. Chang, J. G. Jhu, Y. Y. Li, K. Y. Chen, C. C. Yang, W. S. Chang, L. C. Chen, *ACS Nano* **2014**, *8*, 443.
[27] R. S. Weatherup, L. D'Arsié, A. Cabrero-Vilatela, S. Caneva, R. Blume, J. Robertson, R. Schloegl, S. Hofmann, *J. Am. Chem. Soc.* **2015**, *137*, 14358.
[28] B. Dlubak, M. B. Martin, R. S. Weatherup, H. Yang, C. Deranlot, R. Blume, R. Schloegl, A. Fert, A. Anane, S. Hofmann, P. Seneor, J. Robertson, *ACS Nano* **2012**, *6*, 10930.
[29] V. Zatko, S. M. M. Dubois, F. Godel, M. Galbiati, J. Peiro, A. Sander, C. Carretero, A. Vecchiola, S. Collin, K. Bouzehouane, B. Servet, F. Petroff, J. C. Charlier, M. B. Martin, B. Dlubak, P. Seneor, *ACS Nano* **2022**, *16*, 14007.
[30] P. Martin, B. Dlubak, R. Mattana, P. Seneor, M. B. Martin, T. Henner, F. Godel, A. Sander, S. Collin, L. Chen, S. Suffit, F. Mallet, P. Lafarge, M. L. della Rocca, A. Droghetti, C. Barraud, *Nanoscale* **2022**, *14*, 12692.
[31] M. Piquemal-Banci, R. Galceran, S. M. M. Dubois, V. Zatko, M. Galbiati, F. Godel, M. B. Martin, R. S. Weatherup, F. Petroff, A. Fert, J. C. Charlier, J. Robertson, S. Hofmann, B. Dlubak, P. Seneor, *Nat. Commun.* **2020**, *11*, 5670.
[32] M. Rodriguez-Vega, G. Schwiete, J. Sinova, E. Rossi, *Phys. Rev. B* **2017**, *96*, 235419.
[33] F. Bonell, M. G. Cuxart, K. Song, R. Robles, P. Ordejón, S. Roche, A. Mugarza, S. O. Valenzuela, *Cryst. Growth Des.* **2017**, *17*, 4655.
[34] Z. M. Gebeyehu, A. Arrighi, M. v. Costache, C. M. Sotomayor-Torres, M. J. Esplandiu, S. O. Valenzuela, *RSC Adv.* **2018**, *8*, 8234.
[35] H. Shinotsuka, S. Tanuma, C. J. Powell, D. R. Penn, *Surf. Interface Anal.* **2015**, *47*, 1132.
[36] E. Nolot, C. Sabbione, W. Pessoa, L. Prazakova, G. Navarro, *Appl. Surf. Sci.* **2021**, *536*, 147703.
[37] M. Bianchi, D. Guan, S. Bao, J. Mi, B. B. Iversen, P. D. C. King, P. Hofmann, *Nat. Commun.* **2010**, *1*, 128.
[38] J. Zhang, C. Triola, E. Rossi, *Phys. Rev. Lett.* **2014**, *112*, 096802.
[39] C. D. Spataru, F. Léonard, *Phys. Rev. B* **2014**, *90*, 085115.
[40] P. Lee, K. H. Jin, S. J. Sung, J. G. Kim, M. T. Ryu, H. M. Park, S. H. Jhi, N. Kim, Y. Kim, S. U. Yu, K. S. Kim, D. Y. Noh, J. Chung, *ACS Nano* **2015**, *9*, 10861.
[41] G. Bian, T.-F. Chung, C. Chen, C. Liu, T.-R. Chang, T. Wu, I. Belopolski, H. Zheng, S.-Y. Xu, D. S. Sanchez, N. Alidoust, J. Pierce, B. Quilliams, P. P. Barletta, S. Lorcy, J. Avila, G. Chang, H. Lin, H.-T. Jeng, M.-C. Asensio, Y. P. Chen, M. Z. Hasan, *2D Mater.* **2016**, *3*, 021009.
[42] K. Song, D. Soriano, A. W. Cummings, R. Robles, P. Ordejón, S. Roche, *Nano Lett.* **2018**, *18*, 2033.
[43] S. Jafarpisheh, A. W. Cummings, K. Watanabe, T. Taniguchi, B. Beschoten, C. Stampfer, *Phys. Rev. B* **2018**, *98*, 241402.
[44] K. Zollner, J. Fabian, *Phys. Rev. B* **2019**, *100*, 165141.
[45] D. Kong, J. J. Cha, K. Lai, H. Peng, J. G. Analytis, S. Meister, Y. Chen, H.-J. Zhang, I. R. Fisher, Z.-X. Shen, Y. Cui, *ACS Nano* **2011**, *5*, 4698.
[46] L. v. Yashina, J. Sánchez-Barriga, M. R. Scholz, A. A. Volykhov, A. P. Sirotina, S. N. Vera, M. E. Tamm, A. Varykhalov, D. Marchenko, G. Springholz, G. Bauer, A. Knop-Gericke, O. Rader, *ACS Nano* **2013**, *7*, 5181.
[47] A. J. Green, S. Dey, Y. Q. An, B. O'Brien, S. O'Mullane, B. Thiel, A. C. Diebold, *J Vac Sci Technol A* **2016**, *34*, 061403.
[48] P. A. Sharma, T. Ohta, M. T. Brumbach, J. D. Sugar, J. Michael, *ACS Appl. Mater. Interfaces* **2021**, *13*, 18218.

[49] S. Rajput, Y. Y. Li, M. Weinert, L. Li, *ACS Nano* **2016**, *10*, 8450.
[50] N. Kim, P. Lee, Y. Kim, J. S. Kim, Y. Kim, D. Y. Noh, S. U. Yu, J. Chung, K. S. Kim, *ACS Nano* **2014**, *8*, 1154.
[51] D. Khokhriakov, A. M. Hoque, B. Karpiak, S. P. Dash, *Nat. Commun.* **2020**, *11*, 3657.
[52] A. Zalic, T. Dvir, H. Steinberg, *Phys. Rev. B* **2017**, *96*, 75104.
[53] S. Chen, H. Ji, H. Chou, Q. Li, H. Li, J. W. Suk, R. Piner, L. Liao, W. Cai, R. S. Ruoff, *Adv. Mater.* **2013**, *25*, 2062.
[54] H. Zhou, W. J. Yu, L. Liu, R. Cheng, Y. Chen, X. Huang, Y. Liu, Y. Wang, Y. Huang, X. Duan, *Nat. Commun.* **2013**, *4*, 2096.
[55] A. Ibrahim, G. Nadhreen, S. Akhtar, F. M. Kafiah, T. Laoui, *Carbon N Y* **2017**, *123*, 402.